THE JOURNAL OF PHYSICAL CHEMISTRY A

Article

pubs.acs.org/JPCA

Experimental and Modeling Study of the Reaction C_2F_4 (+ M) ⇔ CF_2 + CF_2 (+ M)

C.J. Cobos,[†] A.E. Croce,[†] K. Luther,[‡] L. Sölter,[‡] E. Tellbach,[‡] and J. Troe[‡,§,*]

[†]INIFTA, Facultad de Ciencias Exactas, Universidad Nacional de La Plata, Argentina

[‡]Institut für Physikalische Chemie, Universität Göttingen, Tammannstrasse 6, D-37077 Göttingen, Germany

[§]Max-Planck-Institut für Biophysikalische Chemie, Am Fassberg 11, D-37077 Göttingen, Germany

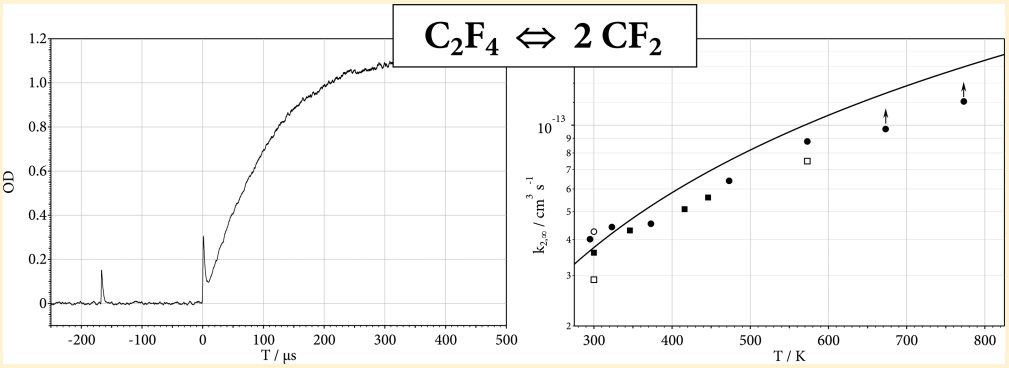

ABSTRACT: The thermal dissociation reaction C_2F_4(+ M) → $2CF_2$(+ M) was studied in shock waves monitoring CF_2 radicals by their UV absorption. The absorption coefficients as functions of wavelength and temperature were redetermined and are represented in analytical form. Dissociation rate constants as functions of bath gas concentration [M] and temperature, from previous and the present work, are presented analytically employing falloff expressions from unimolecular rate theory. Equilibrium constants are determined between 1200 and 1500 K. The data are shown to be consistent, with a C−C bond energy of 67.5 (±0.5) kcal mol^{-1}. High-pressure limiting rate constants for dissociation and recombination are found to be unusually small. This phenomenon can be attributed to an unusually pronounced anisotropy of the potential energy surface, such as demonstrated by quantum-chemical calculations of the potential energy surface.

1. INTRODUCTION

The thermal decomposition of C_2F_4,

$$C_2F_4(+M) \rightarrow 2CF_2(+M) \quad (1)$$

and the reverse recombination of CF_2 radicals,

$$CF_2 + CF_2(+M) \rightarrow C_2F_4(+M) \quad (2)$$

are remarkable in several ways. Unlike the analogous decomposition of C_2H_4, which is dominated by the competing channels[1] $C_2H_4 \rightarrow C_2H_2 + H_2$ and $C_2H_4 \rightarrow C_2H_3 + H$, the decomposition of C_2F_4 proceeds by fission of the C−C bond. Furthermore, in comparison with the recombination of CF_3 radicals forming C_2F_6 with a room temperature high-pressure rate constant[2] of $7.8{\cdot}10^{12}$ cm^3 mol^{-1} s^{-1}, and the recombination of CH_3 radicals forming C_2H_6 with a room temperature high pressure rate constant[3] of $3.5{\cdot}10^{13}$ cm^3 mol^{-1} s^{-1}, the recombination of CF_2 radicals has a room temperature high pressure rate constant as low as[4] $2.4{\cdot}10^{10}$ cm^3 mol^{-1} s^{-1}. One of the aims of the present study is the identification of the reasons for this small value in terms of the properties of the potential energy surface of the C_2F_4 ⇔ $2CF_2$ system.

With increasing temperature, reaction 2 should increasingly deviate from low-temperature, high-pressure behavior. The first indications of this were found in the recombination study of ref 4 near 900 K. Further increasing the temperature, the dissociation reaction 1 has generally been found to be far from the limiting high-pressure regime.[5] Then a representation of the complete temperature- and pressure-dependence of the rate constant, k_1, over the full falloff range of the reaction needs to be elaborated. First steps in this direction have been made in the dissociation study of ref 5. In other dissociation experiments, such as refs 6−9, oversimplified assumptions about the pressure dependence of reaction 1 were made. The problem of the pressure dependence did not have to be accounted for in most of the recombination studies, such as refs 4 and 10−16, which were generally performed under conditions such that limiting high-pressure, second-order behavior was observed. It is the second goal of the present work to analyze the available dissociation and recombination data in terms of unimolecular rate theory. The results of this analysis are representations of the temperature and pressure dependences of k_1 and k_2 over their full falloff ranges

Received: August 21, 2013
Revised: October 4, 2013
Published: October 8, 2013

(k_1 is defined through $d[C_2F_4]/dt = -k_1[C_2F_4]$, whereas k_2 is defined as $d[C_2F_4]/dt = k_2[CF_2]^2$).

The analysis of k_1 and k_2 is based on the molecular parameters of C_2F_4 and CF_2. Of particular importance is the dissociation energy, E_0, of C_2F_4, which strongly influences k_1. At the same time, the molecular parameters, particularly E_0, are contained in the equilibrium constant

$$K_c = k_1/k_2 \quad (3)$$

Our analysis, thus, has to be internally consistent and reproduce k_1, k_2, and K_c at the same time. Previous measurements of K_c differed considerably.[5,7,9] The reasons for this were different and internally inconsistent UV absorption coefficients of the monitored CF_2 radicals. In addition, reaction 1 generally was studied under conditions where the dissociation was not complete such that part of the measurements of k_1 were also affected by uncertainties in K_c and in the absorption coefficients of CF_2. For this reason, we have remeasured CF_2 absorption coefficients together with dissociation rate constants k_1 and equilibrium constants K_c. Our results for the absorption coefficients are consistent with the most general previous results from ref 4 and, particularly, from ref 17. However, they differ slightly from the results of refs 5 and 9 and more strongly from refs 7 and 8. Redetermining K_c with correct absorption coefficients, therefore, was an important aspect of our work.

Analyzing K_c leads to the enthalpy of the reaction ΔH_R^0 which may be compared with other experimental determinations and results from quantum-chemical calculations. The dissociation energy, E_0, of C_2F_4, here given by the reaction enthalpy $\Delta H_{R,0}^0$ at 0 K, is related to the heats of formation of CF_2 and C_2F_4 at 0 K through

$$E_0 = \Delta H_{R,0}^0 = 2\Delta H_{f,0}^0(CF_2) - \Delta H_{f,0}^0(C_2F_4) \quad (4)$$

Although earlier tabulations, such as ref 18 used $\Delta H_{f,0}^0(C_2F_4) = -156.6$ kcal mol^{-1} (similar to the value of -157.5 kcal mol^{-1} recommended in ref 19), more recent evaluations[20−22] have led to an experimental value of $\Delta H_{f,0}^0(C_2F_4) = -161.0$ kcal mol^{-1}. This is in close agreement with the recent high-level ab initio calculation in ref 23, which gave -160.5 kcal mol^{-1}. Combining the latter value for $\Delta H_{f,0}^0(C_2F_4)$ with $\Delta H_{f,0}^0(CF_2)$ from ab initio calculations of ref 24 yielding $\Delta H_{f,0}^0(CF_2) = -46.6$ kcal mol^{-1} (close to the value of -46.2 kcal mol^{-1} from ref 25 and similar values from refs 26 and 27) leads to $E_0 = 67.3$ kcal mol^{-1}. On the other hand, $\Delta H_{f,0}^0(CF_2) = -45.82$ kcal mol^{-1} was recommended in ref 21, which, with $\Delta H_{f,0}^0(C_2F_4) = -160.59$ kcal mol^{-1} from the same reference, gives $E_0 = 68.9$ kcal mol^{-1}. With NIST-JANAF values,[19] one would have obtained $E_0 = 69.4$ kcal mol^{-1}. There is, thus, still a considerable uncertainty of the relevant value of E_0. As the corresponding differences at temperatures in the range 1100−1600 K of the present work amount to up to a factor of 2 in the factor $\exp(-E_0/RT)$, the effects of changing E_0 should become detectable in our analysis of k_1, k_2, and K_c. It is, therefore, a third goal of this article to compare calculated K_c and modeled k_1 and k_2 with experimental results using E_0 as a fit parameter. In this way, an experimental value for E_0 can be established, and consistency between experimental and theoretical values of E_0 can be tested.

2. EXPERIMENTAL TECHNIQUE AND RESULTS

In our work, we have remeasured C_2F_4 dissociation rates by monitoring UV absorption signals from CF_2 radicals, that is, we have used the same experimental technique as applied in refs 5 and 7−9, although improvements in data acquisition were possible. Because part of the measurements of k_1 and all determinations of K_c depended on the correct concentrations of CF_2, particular care was taken to have correct absorption coefficients, ε, of CF_2.

We worked with incident and reflected shock waves in a shock tube that has been described before.[28,29] Because most details of the technique have been reported,[29] they need not be repeated here. We used reaction mixtures with <600 ppm of C_2F_4 in Ar and studied the reaction over the temperature range 1000−1700 K with Ar concentrations in the range 10^{-5}−10^{-4} mol cm^{-3}. Argon of high purity (99.9999% from Air Liquide) was employed. C_2F_4 (>99% from Dyneon GmbH) contained some α-pinene to prevent polymerization; this was removed by repeated freezing (oxygen and water traces were removed by use of oxysorb cartridges from Air Liquide). Because only very low concentrations of C_2F_4 in Ar were employed, these traces did not play any role in our experiments.

Figures 1 and 2 show typical absorption profiles of CF_2, such as recorded at 248 nm behind reflected and incident shock waves.

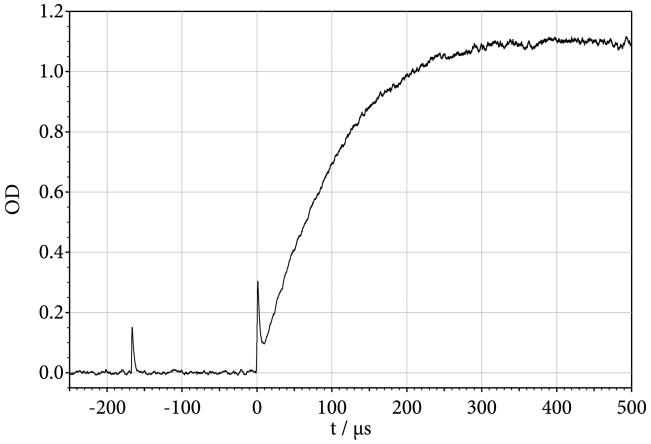

Figure 1. Formation of CF_2 in the thermal dissociation of C_2F_4 behind a reflected shock wave (the Schlieren peaks denote the arrival of the incident and reflected shock; 570 ppm of C_2F_4 in Ar; reflected shock: $T = 1271$ K and $[Ar] = 1.1\cdot10^{-4}$ mol cm^{-3}; $OD = \varepsilon\cdot x\cdot[CF_2]$ with $x = 9.4$ cm and ε (248) $= 3.2\cdot10^6$ cm^2 mol^{-1}, incomplete dissociation with $\alpha = 27\%$; see text).

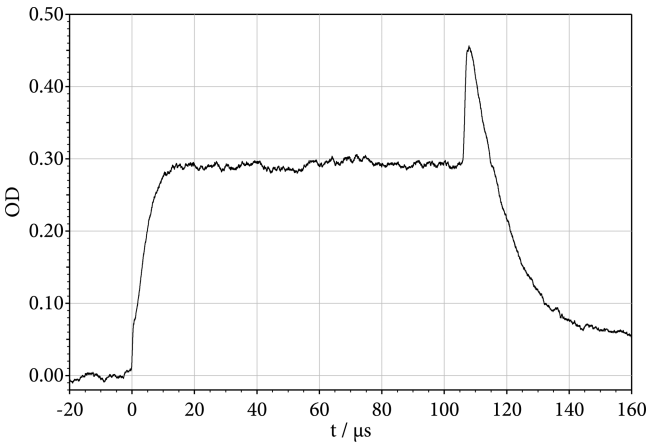

Figure 2. Formation of CF_2 in the thermal dissociation of C_2F_4 behind incident shock wave (560 ppm of C_2F_4 in Ar; incident shock: $T = 1658$ K, $[Ar] = 1.1\cdot10^{-5}$ mol cm^{-3}, ε (248 nm) $= 2.7\cdot10^6$ cm^2 mol^{-1}. reflected shock: $T = 3503$ K, $[Ar] = 2.5\cdot10^{-5}$ mol cm^{-3}, ε (248 nm) $= 2.1\cdot10^6$ cm^2 mol^{-1}; for dissociation of CF_2, see ref 29).

dx.doi.org/10.1021/jp408363s | J. Phys. Chem. A 2013, 117, 11420−11429

The concentration profiles always followed first-order rate laws for the dissociation 1, and second-order rate laws for the recombination 2 when the decomposition was incomplete and approached equilibrium. Because only the reaction product CF_2 was monitored, in the latter case, the evaluation of k_1, k_2, and K_c required accurate knowledge of the absorption coefficients ε of CF_2 and careful specification of the composition of the reaction mixture. Because the temperature for Figure 1 was too low to show any CF_2 formation behind the incident wave, CF_2 was formed only behind the reflected wave. A determination of the equilibrium constant K_c from the final CF_2 absorption signal, as well as of the rate constant k_2 for C_2F_4 decomposition, thus required the accurate knowledge of the absorption coefficient of CF_2. Under the shown conditions, about 27% of the parent C_2F_4 decomposed until equilibrium. For the higher temperatures of Figure 2, C_2F_4 decomposes nearly completely behind the incident shock wave. The formed CF_2 finally decomposes behind the reflected wave, such as studied in ref 29. (One should note that the time axis behind the incident shock is compressed by the factor 3.3, that is, by the ratio of densities before and behind the incident shock front; on the other hand, the time scale behind the reflected shock corresponds to laboratory time. The determination of k_1 from Figure 2 does not require knowledge of the absorption coefficient.)

2.1. Absorption Coefficients of CF_2. A useful guide to the temperature and wavelength dependence of ε (base e) were the measurements from ref 17, which corrected earlier data from refs 7 and 8. Figures 3 and 4 compare our new determinations of ε (data from C_2F_4 and CHF_3 precursors for CF_2 are included) with the older data from ref 17 and results from refs 4 and 9. In addition, a comparison of the results with a two-dimensional extension of the Sulzer–Wieland equation (eq A5 of ref 30) is shown; that is, we use a representation (base e for ε),

$$\varepsilon(\nu, T) \approx \varepsilon_{max} F^{n/2} \exp[-nF[(\nu - \nu_0)/(\Delta\nu_0)]^2] \quad (5)$$

with $F = \tanh(\Theta_0/2T)$ and the fitted parameters $\varepsilon_{max} = 1.07 \times 10^7$ cm^2 mol^{-1}, $n = 2$, $\nu_0 = 40\,300$ cm^{-1}, $\Delta\nu_0 = 1100$ cm^{-1} and $\Theta_0 = 960$ K. It may appear surprising that a highly structured spectrum, like that of CF_2 near 300 K (see ref 4), with increasing temperature approaches a continuous form such as given by eq 5; however, the same behavior was also observed in ref 30 for UV absorption spectra of other polyatomic molecules. Unlike ref 9, we used a variety of CF_2 precursors whose reactions will be described in separate publications (among the precursors studied were CF_3H, CF_2H_2, C_2F_5H, C_3F_7H, and C_2F_4; here, only data from CF_3H and C_2F_4 are included). The temperature dependence of ε at the absorption maximum, such as illustrated in Figure 4, fairly well agrees among refs 4, 9, 17 and the present work. The determinations of ε in refs 5, 7, and 8 are less consistent with Figure 4 and, thus, are discarded. The consequences of incorrect ε on measurements of k_1 and, in particular, of K_c in these earlier studies sometimes were serious; sometimes, they were less critical (see below).

Although the two-dimensional extended Sulzer–Wieland representation of ε (ν, T) leads to a quite satisfactory fit of the experimental data, in reality, one cannot expect perfect agreement. Indeed, minor discrepancies become apparent in Figure 4 where data for 248 nm over a very wide temperature range are compared with eq 5. Empirically, we found that an even better representation of ε (ν, T) for fixed ν than by eq 5 can be obtained with a Gaussian-type expression,

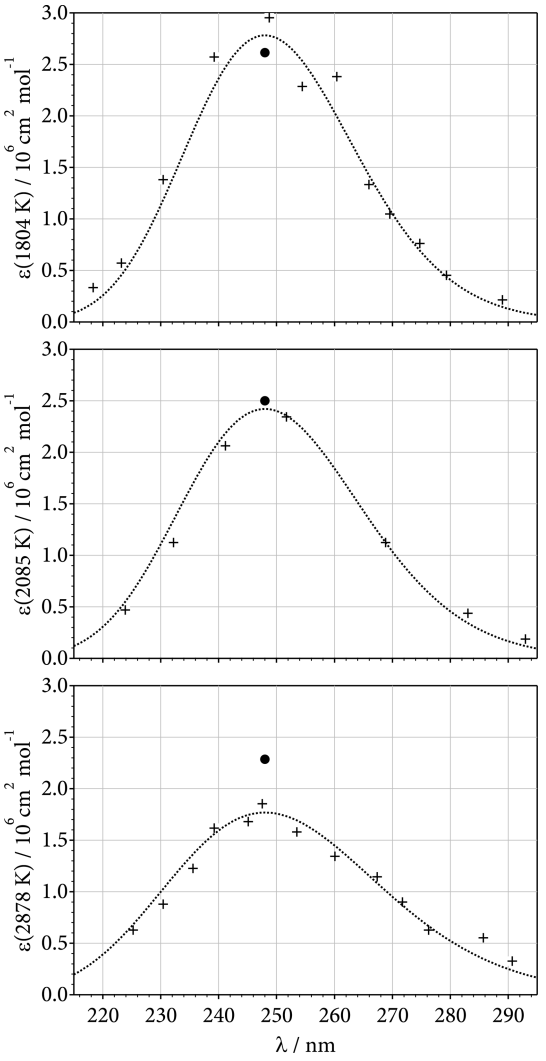

Figure 3. Absorption coefficients ε (base e) for CF_2 (experimental data: +, [17]; ●, present work; dashed curves, fit by eq 5. From top to bottom: T = 1804, 2085, and 2878 K.

$$\varepsilon(\lambda = 248 \text{ nm}, T)/\text{cm}^2\text{mol}^{-1} \approx 3.35\cdot10^6 + 4.6\cdot10^7 \exp\{-[(T + 1457\text{ K})/1272\text{ K}]^2\} - 245(T/\text{K}) \quad (6)$$

We estimate the uncertainty of ε from eq 6 to be about ±10%. The great effort to have accurate values of ε became necessary for situations when CF_2 yields from various precursor molecules were of quantitative interest (see separate publications for the molecules mentioned above).

2.2. Equilibrium Constants, K_c. Whenever dissociation equilibria could be measured within the available experimental time of ~1 ms (see Figure 1), equilibrium constants, K_c, were derived from the dissociated fraction, α, of the initial C_2F_4 concentration $[C_2F_4]_0$ through

$$K_c = [C_2F_4]_0 4\alpha^2/(1 - \alpha) \quad (7)$$

Table 1 summarizes experimental conditions and measured values of K_c. Figure 5 shows a van't Hoff plot of K_c and compares present results with modeled values. The figure also includes results from refs 5 and 9. The results from ref 5 were reevaluated with the absorption coefficients ε from the present work as represented by eq 6. The small differences between the

dx.doi.org/10.1021/jp408363s | J. Phys. Chem. A 2013, 117, 11420–11429

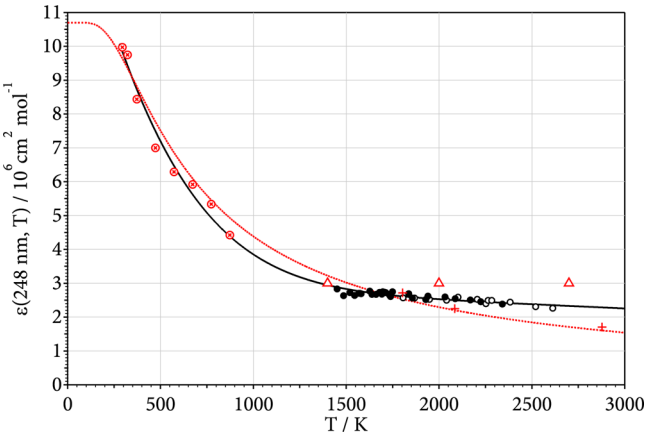

Figure 4. Absorption coefficients ε (base e) for CF_2 at 248 nm (experimental data: ●, present work, from C_2F_4; ○, present work, from CHF_3; ⊗, [**4**]; Δ, [**5**]; +, [**17**]; dotted curve, fit by eq 5; full curve, fit by eq 6; see text).

Table 1. Representative Experimental Results for Equilibrium Constants K_c and Rate Constants k_1 of the Reaction $C_2F_4 \rightarrow 2CF_2$[a]

T/K	[Ar]/mol cm^{-3}	K_c/mol cm^{-3}	k_1/s^{-1}
1100	$2.4\cdot10^{-5}$		$3.7\cdot10^{1}$
1123	$2.3\cdot10^{-5}$		$6.5\cdot10^{1}$
1128	$2.3\cdot10^{-5}$		$9.3\cdot10^{1}$
1161	$2.3\cdot10^{-5}$		$1.6\cdot10^{2}$
1170	$1.2\cdot10^{-4}$	$1.9\cdot10^{-9}$	$2.9\cdot10^{2}$
1172	$2.2\cdot10^{-5}$		$1.2\cdot10^{2}$
1174	$2.0\cdot10^{-5}$		$1.5\cdot10^{2}$
1215	$1.1\cdot10^{-4}$		$9.0\cdot10^{2}$
1224	$1.9\cdot10^{-5}$		$4.3\cdot10^{2}$
1226	$2.0\cdot10^{-5}$		$7.1\cdot10^{2}$
1271	$1.1\cdot10^{-4}$	$2.0\cdot10^{-8}$	$2.1\cdot10^{3}$
1329	$9.8\cdot10^{-5}$	$6.9\cdot10^{-8}$	$4.2\cdot10^{3}$
1367	$9.8\cdot10^{-5}$	$1.4\cdot10^{-7}$	$8.9\cdot10^{3}$
1383	$9.7\cdot10^{-5}$	$2.4\cdot10^{-7}$	$1.4\cdot10^{4}$
1450	$9.1\cdot10^{-5}$	$7.0\cdot10^{-7}$	$5.3\cdot10^{4}$
1486	$9.0\cdot10^{-5}$	$1.3\cdot10^{-6}$	$4.5\cdot10^{4}$
1540	$1.3\cdot10^{-5}$		$4.7\cdot10^{4}$

[a]See text.

absorption coefficients used in refs 5 and 9 have some relevance for a second-law analysis of K_c, but are less serious for a third-law analysis (see the following). We evaluated our data by calculating K_c in rigid rotor-harmonic oscillator approximation (like in ref 19), using frequencies and rotational constants for C_2F_4 and CF_2 from refs 18 and 31−33 (see Appendix) and fitting $E_0 = \Delta H^0_{R,0}$. We obtained

$$\Delta H^0_{R,0} = 67.5(\pm0.5)\ \text{kcal mol}^{-1} \quad (8)$$

where the uncertainty accounts for the differences between the data shown in Figure 5. (We note that the earlier third-law analysis of ref 5 led to $\Delta H^0_{R,298} = 68.8(\pm1.7)$ kcal mol^{-1}, corresponding to $\Delta H^0_{R,0} = 67.8$ kcal mol^{-1}, and that of ref 9 led to $\Delta H^0_{R,298} = 68.4(\pm0.45)$ kcal mol^{-1}, corresponding to $\Delta H^0_{R,0} = 67.4$ kcal mol^{-1}.) Because the most recent ab initio calculations from refs 23 and 24 led to $\Delta H^0_{R,0} = 67.3(\pm0.6)$ kcal mol^{-1}, experimental and theoretical values of K_c and of $E_0 = \Delta H^0_{R,0}$ appear to be of satisfactory internal consistency now, favoring a lower value of E_0 than recommended in ref 21.

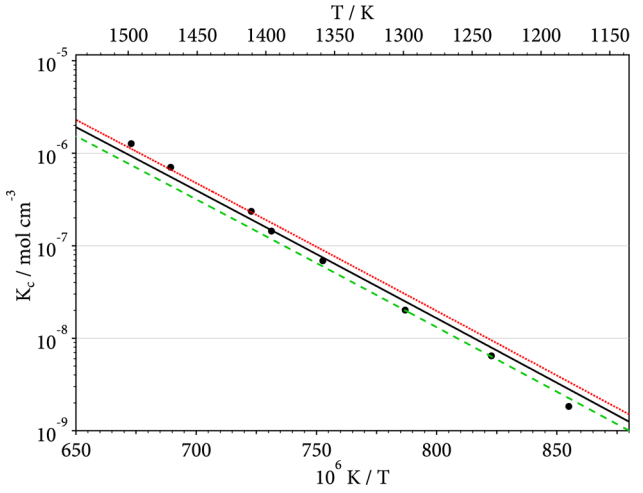

Figure 5. Equilibrium constants $K_c = [C_2F_4]/[CF_2]^2$ (experimental data: ●, present work; dotted curve, [**9**]; dashed curve, [**5**] reevaluated with ε from the present work (see text); solid curve, modeling from present work with $\Delta H^0_0 = 67.5$ kcal mol^{-1}).

Our modeled equilibrium constants, K_c, of Figure 5 over the range 300−2000 K can be fitted in the form

$$K_c = 7.56\cdot10^{5}(T/300\ \text{K})^{-2.4}\ \exp(-35050\ \text{K}/T)\ \text{mol cm}^{-3} \quad (9)$$

which reproduces the calculations within better than 1% over the range 1000−1500 K of interest here. Our measurements are scattered around eq 9, as shown in Figure 5. The figure also includes the results from ref 9, (without corrections because the used ε corresponds to eq 6) and the results from ref 5 (after reevaluation with a slightly modified ε as given by eq 6). The factor $7.56\cdot10^5$ in eq 9 of ref 9 would change to $9.05\cdot10^5$, and for ref 5, to $6.04\cdot10^5$, such that K_c from eq 9 finally should be accurate within about ±20%. This translates into the ±0.5 kcal mol^{-1} uncertainty of the fitted E_0, as indicated in eq 8.

We note that K_c (1200 K) = $5.6\cdot10^{-9}$ mol cm^{-3} from eq 9 is in fair agreement with a value of K_c (1200 K) = $7.2\cdot10^{-9}$ mol cm^{-3} from ab initio calculations of ref 34. On the other hand, ref 19 would have led to K_c (1200 K) = $2.7\cdot10^{-9}$ mol cm^{-3}, and refs 20 and 21 would have given K_c (1200 K) = $3.1\cdot10^{-9}$ mol cm^{-3}. We also note that our modeled entropies, such as those included in the modeled K_c of eq 9, agree with the values given in ref 18; that is, $S°_{298}(C_2F_4) = 71.7$ cal K^{-1} mol^{-1} and $S°_{298}(CF_2) = 57.6$ cal K^{-1} mol^{-1}.

2.3. Dissociation Rate Constants, k_1. First-order rate constants, k_1, could be obtained directly from CF_2 absorption profiles such as Figures 1 and 2. At higher temperatures (T > 1400 K), the decomposition was nearly complete such that the results were independent of the value of ε; at lower temperatures (T < 1400 K), the slopes of the rise of absorption had to be evaluated such that the results depended on ε. It was, therefore, essential to have the correct value of ε, such as described in Section 2.1. Table 1, in addition to K_c, includes representative measured values of k_1. Because the rate constants depend on both the temperature, T, and the argon concentration [Ar], Figures 6−8 show falloff curves for the fixed temperatures 1200, 1400, and 1600 K. Measurements at temperatures slightly off these reference values were interpolated using the [Ar]-dependent temperature coefficients of the modeled rate constants given below.

The figures include modeled falloff curves such as described below together with the limiting low- and high-pressure rate

dx.doi.org/10.1021/jp408363s | J. Phys. Chem. A 2013, 117, 11420−11429

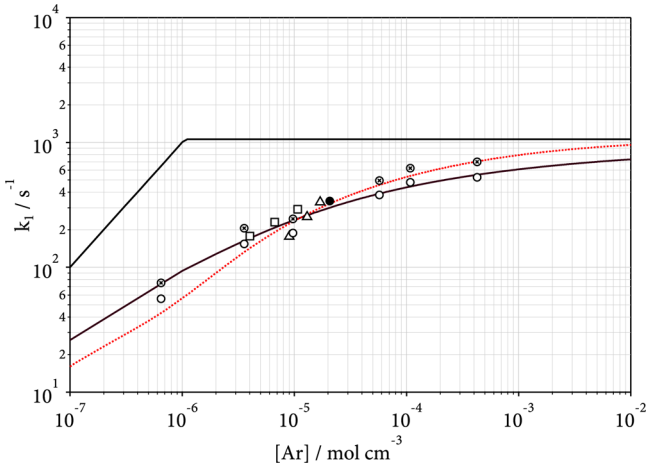

Figure 6. Falloff curve for $C_2F_4 \rightarrow 2CF_2$ at T = 1200 K (experimental data: ○, [**5**]; □, [**9**]; Δ, [7]; ●, present work; red line, modeling with eq 20 with limiting low- and high-pressure rate constants $k_{1,0}$ and $k_{1,\infty}$, respectively, as shown in the figure and given in Table 4; black line, modeling with eq 19 with $k_{1,0}$ increased by a factor of 3 compared with Table 4).

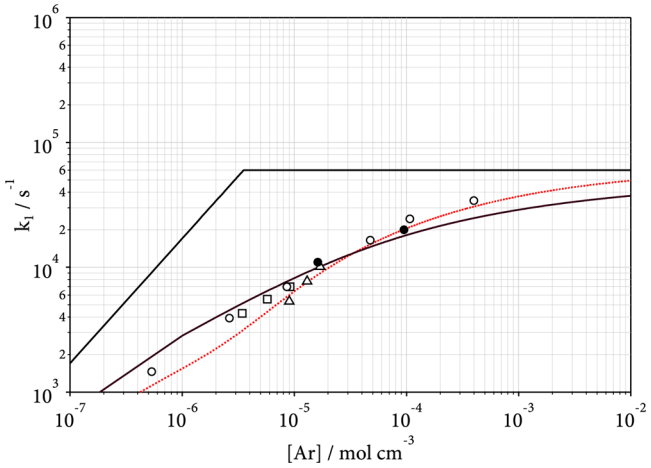

Figure 7. As Figure 6, for T = 1400 K.

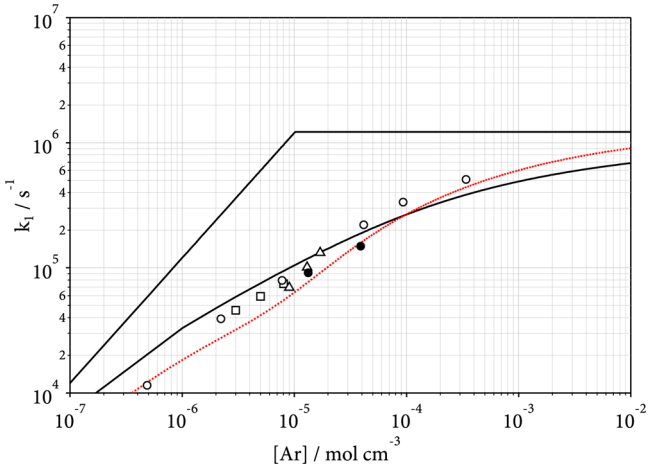

Figure 8. As Figure 6, for T = 1600 K.

constants. One realizes that the measurements of k_1 were all done in the intermediate falloff range close to the center of the falloff curves. Measurements from refs 5, 7, and 9 are included and found to be in good agreement with the present data. However, the assumed pressure dependences of refs 7 and 9 had to be abandoned (data from ref 5 for 1200 K were reevaluated with corrected absorptions coefficients, such as indicated in Figure 7). Analytical representations of k_1 (T, [Ar]) are described in Section 4. The apparent problems of representing the experimental falloff curves by the given analytical expressions will also be commented on.

3. MODELING OF RATE CONSTANTS

The rate constants k_1 (T, [Ar]) depend on intramolecular dynamics, as determined by the properties of the potential energy surface, and on intermolecular collisional energy transfer. In the following, we present a modeling of the rate constants in terms of these processes, demonstrating which parameters can be estimated at least semiquantitatively and which have to be left as fitted quantities. At this stage, the high-pressure rate constants become calculable from an ab initio characterization of the global properties of the potential, whereas the low-pressure rate constants require the choice of a fitted parameter, that is, the average energy, $\langle \Delta E \rangle$, transferred per collision. In the following, we first consider high-pressure rate constants $k_{1,\infty}$ or $k_{2,\infty}$ after having characterized the potential, then proceed to low-pressure rate constants $k_{1,0}$ or $k_{2,0}$ and, finally, represent rate constants in the intermediate falloff range.

3.1. Relevant Properties of the Potential. High-pressure recombination is understood as a capture process which in our work is treated by the SACM/CT (statistical adiabatic channel model/classical trajectories) approach of ref 35. In this treatment, attention is focused on the dynamics of the transitional modes as characterized by classical trajectories on an anisotropic model potential. To use this method for estimating the rate constant $k_{2,\infty}$, one has to explore the $F_2C{-}CF_2$ potential along the minimum energy path (MEP). We used various quantum-chemical methods, such as (i) density functional theory (DFT) on the B3LYP/6-311+G(3df) level, (ii) MP2/6-311+G(3df), (iii) CBS-QB3 (i.e., MP2/CBS on a B3LYP/6-311G(d) geometry), and (iv) G4 (i.e., CCSD(T)/CBS on a B3LYP/6-31G(2df,p) geometry). All calculations were performed with the Gaussian 09 package.[36]

We first consider the MEP potential. Figure 9 compares the results of various calculations. Selecting the G4 curve, in Figure 10, we compare the results with standard Morse potentials. We note

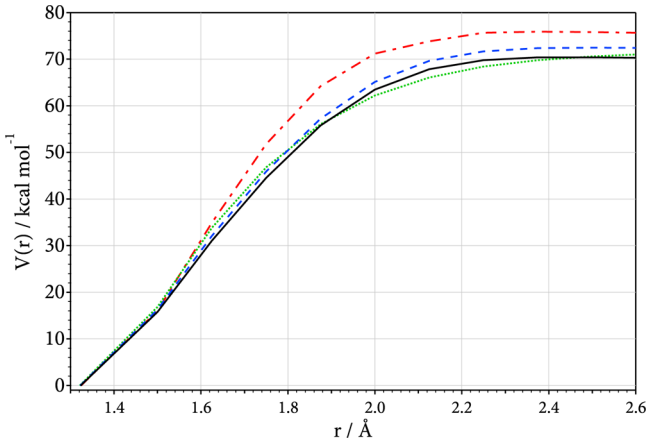

Figure 9. MEP energy $V(r)$ for $C_2F_4 \rightarrow 2CF_2$ (calculations from this work at different levels of theory: -·-·-, MP2/6-311+G(3df); ·····, B3LYP/6-311+G(3df); -----, CBS-QB3; —, G4 ;see text).

dx.doi.org/10.1021/jp408363s | J. Phys. Chem. A 2013, 117, 11420−11429

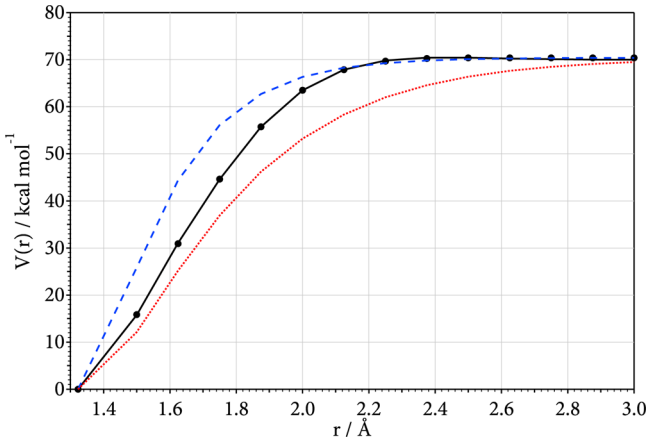

Figure 10. MEP energy $V(r)$ for $C_2F_4 \rightarrow 2CF_2$ (calculations from this work: ●, by G4; —, modified Morse potential with $\beta(r)$ from eq 10; ·····, Morse potential with $\beta = 3.0$ Å^{-1}; -----, Morse potential with $\beta = 5.2$ Å^{-1}; see text).

that the latter considerably differ from the G4 results, particularly if the standard Morse parameter, $\beta = 3.0$ Å^{-1} (from a C−C force constant[37] of 8.9 μdyn Å^{-1}), is employed. For long range, $\beta = 5.2$ Å^{-1} would give better agreement with the G4 results. The G4 results formally can be represented by a Morse potential with a C−C bond length (r)-dependent Morse parameter,

$$\beta(r)/\text{Å}^{-1} = 3.876 - 2.422(r - r_e)/\text{Å} + 4.722(r - r_e)^2/\text{Å}^2 \qquad (10)$$

where $r_e = 1.321$ Å. Along the MEP, the molecule changes its structure from a planar to an anticonfiguration with the angle δ between the CF_2 planes and the original plane increasing from 0° to about 67° at large r (e.g., δ = 0°, 40°, 59°, and 65° for r/Å = 1.321, 1.625, 2.0, and 2.5, respectively) (see Figure 11).

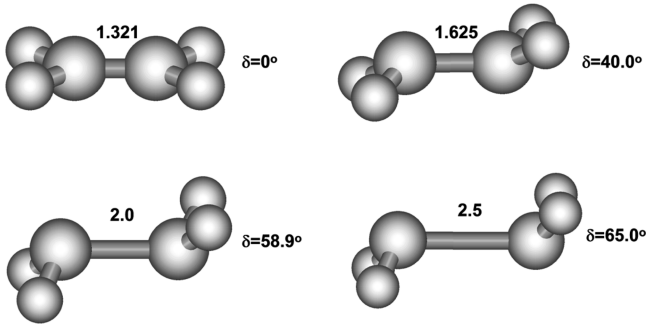

Figure 11. C_2F_4 structures along the MEP for $C_2F_4 \rightarrow 2CF_2$ (calculations from this work at the B3LYP/6-311+G(3df) level) for $r = 1.321$, 1.625, 2.0, and 2.5 Å, respectively; δ = C−CF_2 angle; see text).

This behavior can be represented by effective r-dependent rotational constants,

$$(A + B)/2\ \text{cm}^{-1} = 0.0869[1 + 0.333(r - r_e)/\text{Å} + 0.166(r - r_e)^2/\text{Å}^2]^{-1} \qquad (11)$$

(from B3LYP/6-311+G(3df) calculations). It is important to have eq 11 because it is required for a determination of the centrifugal barriers of the reaction, which are important quantities in the low-pressure as well as the high-pressure rate constants (see below).

The anisotropy of the potential can be characterized by the dependence of the harmonic vibrational frequencies ν_{tors} of the torsional modes of C_2F_4 on the C−C bond length, r. With increasing r, these transitional modes change from vibrations into free rotations of the CF_2 fragments. The interplay between the radial potential, characterized by eq 10, and the anisotropy of the potential, characterized by the r dependence of the ν_{tors}, governs the "dynamical hindrance" of the capture process (see below). At short-range, for $r < 1.7$ Å, the r dependence of the various ν_{tors} looks irregular; however, at $r > 1.7$ Å, the decrease of the ν_{tors} (r) with increasing r is nearly exponential, such as observed frequently. Figure 12 illustrates this behavior as obtained from

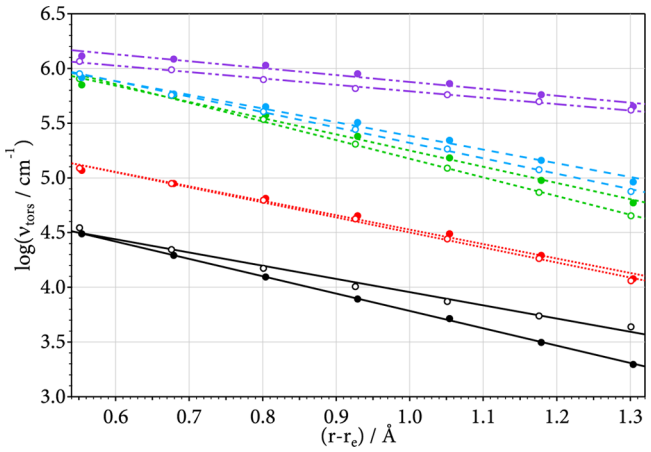

Figure 12. Frequencies ν_{tors} for five transitional modes along the MEP for $C_2F_4 \rightarrow 2CF_2$ (calculations from this work at the B3LYP/6-311+G(3df) level (●) and at the MP2/6-311+G(3df) level (○); the looseness parameters α in Å^{-1}, from top to bottom, are 0.629, 1.25, 1.48, 1.32, and 1.58 for ● and 0.585, 1.41, 1.71, 1.37, and 1.21 for ○; see text).

B3LYP (method i) and MP2 (method ii) calculations. We describe the decay in terms of anisotropy parameters, α,[38] with

$$\nu_{tors} \propto \exp[-\alpha(r - r_e)] \qquad (12)$$

such as given in the figure. Average values of α are 1.19 (B3LYP) and 1.26 (MP2) Å^{-1}. Because the relevant centrifugal barriers are located at long range, the effective Morse parameter according to Figure 10 can be estimated as $\beta \approx 5.2$ Å^{-1}, such that the ratio α/β is close to

$$\alpha/\beta = 0.23 \qquad (13)$$

This is an unusually low value of the ratio α/β (see, e.g., ref 39). The small value of the ratio indicates a "rigid effective activated complex situation". For ratios α/β approaching unity, loose activated complex theory (i.e., phase space theory, PST) would be approached, whereas $\alpha/\beta \rightarrow 0$ would lead to a rigid activated complex, RRKM (Rice−Ramsperger−Kassel−Marcus)-type theory.[39] The small value of the experimental high pressure recombination rate constant, $k_{2,\infty}$, thus can be attributed to the unusually pronounced anisotropy of the potential as characterized by the small value of the ratio α/β given by eq 13.

3.2. High-Pressure Rate Constants. As long as sufficiently accurate ab initio calculations of the complete potential are not available, we proceed with the semiquantitative SACM/CT approach of ref 35 using the characteristic potential properties described in section 3.1. On the basis of a given ratio, α/β, in this work, the association of two quasi-linear identical species forming a linear adduct in a model valence potential was treated. This is the simplified situation chosen here. (This model appears adequate enough for the calculation of the "rigidity factors, f_{rigid}" of the process, i.e., of the factors accounting for the transition of the free rotations of the radicals into the bending vibrations of the

dx.doi.org/10.1021/jp408363s | J. Phys. Chem. A 2013, 117, 11420−11429

Table 2. Modeled High Pressure Rate Constants for Dissociation and Recombination $k_{1,\infty}$ and $k_{2,\infty}$, Respectively, and Equilibrium Constants K_c for $C_2F_4 \Rightarrow 2CF_2$[a]

T/K	$k_{1,\infty}$/s^{-1}	$k_{2,\infty}$/cm^3 mol^{-1} s^{-1}	K_c/mol cm^{-3}	$k_{2,\infty}^{PST}$/cm^3 mol^{-1} s^{-1}	f_{rigid}
300		$2.20\cdot10^{10}$		$1.22\cdot10^{14}$	$1.8\cdot10^{-4}$
1000	3.55	$1.41\cdot10^{11}$	$2.52\cdot10^{-11}$	$2.15\cdot10^{14}$	$6.6\cdot10^{-4}$
1250	$3.28\cdot10^{3}$	$1.98\cdot10^{11}$	$1.66\cdot10^{-8}$	$2.38\cdot10^{14}$	$8.3\cdot10^{-4}$
1500	$3.01\cdot10^{5}$	$2.62\cdot10^{11}$	$1.15\cdot10^{-6}$	$2.60\cdot10^{14}$	$1.0\cdot10^{-3}$
1750	$7.36\cdot10^{6}$	$3.32\cdot10^{11}$	$2.22\cdot10^{-5}$	$2.79\cdot10^{14}$	$1.2\cdot10^{-3}$
2000	$7.92\cdot10^{7}$	$4.08\cdot10^{11}$	$1.94\cdot10^{-4}$	$2.97\cdot10^{14}$	$1.4\cdot10^{-3}$

[a]See text.

adduct. Calculations assuming a nonlinear adduct, which was also treated in ref 35, led to similar results. Neglecting the transition of the third of the free rotations of nonlinear CF_2 into two low-frequency torsions of CF_2 in C_2F_4 is justified because it has only little influence on adiabatic channel potential curves.) A Morse-type MEP potential in the modeling is combined with an anisotropic angular potential corresponding to eq 12. Because the temperatures of interest are much larger than the characteristic temperatures of the free reactant rotor/torsional adduct oscillator modes, classical trajectories can be used to follow the association process. The results were represented analytically in section IV of ref 35. Our present work used the derived relationships.

Table 2 summarizes the results of our modeling. In addition to $k_{2,\infty}$, K_c, and $k_{1,\infty}$, the results from phase space theory ($\alpha/\beta \gg 1$, $k_{2,\infty}^{PST}$) and the "rigidity factors" $f_{rigid} = k_{2,\infty}/k_{2,\infty}^{PST}$ are given. Our results can be approximated by eq 9 and

$$k_{2,\infty} = 2.26\cdot10^{10}(T/300\ \mathrm{K})^{1.53}\ \mathrm{cm^3\ mol^{-1}\ s^{-1}} = 3.75\cdot10^{-14}(T/300\ \mathrm{K})^{1.53}\ \mathrm{cm^3\ s^{-1}} \quad (14)$$

$$k_{1,\infty} = 1.71\cdot10^{16}(T/300\ \mathrm{K})^{-0.87}\exp(-35050\mathrm{K}/T)\ \mathrm{s^{-1}} \quad (15)$$

The results of eq 14 for $k_{2,\infty}$ agree surprisingly well with the experimental data from refs 4 and 10−12 (see Figure 13).

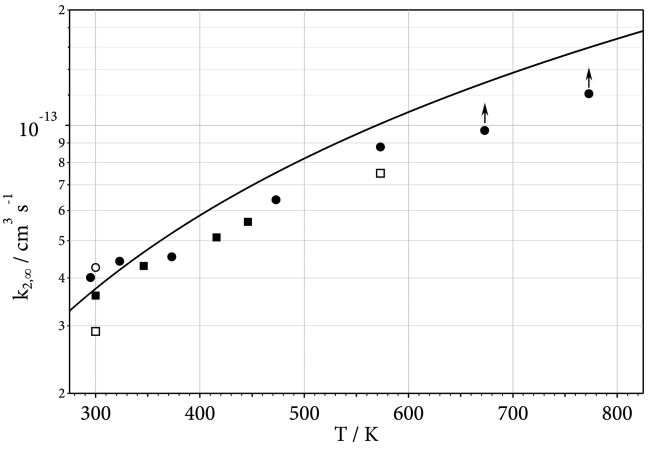

Figure 13. High pressure recombination rate constants $k_{2,\infty}$ for $2CF_2 \rightarrow C_2F_4$ (experimental data: ●, [4] there may be falloff in the results above 650 K (see text); □, [10]; ■, [11]; ○, [12]; solid curve, modeling from the present work, represented by eq 13; see text).

(Data from ref 6 are excluded as discussed in ref 40; more data at room temperature, as from refs 10, 13, and 41, agree with the shown results.) Both the absolute values and temperature coefficients are reasonably well reproduced. We take this agreement as an indication that the modeling, which so far was free from fit parameters, at least semiquantitatively explains the high-pressure rate constants. It, therefore, also reveals the origin of the small values of the high-pressure rate constants in terms of the properties of the potential (see above).

3.3. Low-Pressure Rate Constants. The limiting low-pressure rate constants $k_{1,0}$ and $k_{2,0}$ include the average energy transferred per collision $\langle\Delta E\rangle$ between excited C_2F_4 and the bath gas, Ar (and the related collision efficiency β_c), which remains a parameter to be fitted from the experimental results. In our analysis, we follow the standard formalism outlined in ref 42. Table 3 summarizes factors entering the rate constants $k_{1,0}$. We employ the nomenclature of ref 42. In detail, we determine the rotational factors, F_{rot}, with centrifugal barriers on the basis of eq 11 and derived from the MEP potential. The required molecular parameters are again given in the Appendix. The vibrational harmonic density of states $\rho_{vib,h}(E_0)$ follows as 2.48×10^{10}/kcal mol^{-1}. Less certain is the anharmonicity factor, F_{anh}, which, analogous to refs 43 and 44, is estimated as 1.7. Our modeled strong collision rate constant can be represented by

$$k_{1,0}^{SC} = [\mathrm{Ar}]2.45\cdot10^{28}\ (T/300\ \mathrm{K})^{-8.70}\exp(36660\ \mathrm{K}/T)\ \mathrm{cm^3\ mol^{-1}\ s^{-1}} \quad (16)$$

Including weak collision efficiencies $\beta_c = k_{1,0}^{SC}$, such as fitted from the measured falloff curves (see below), over the range of 1200−1600 K, we obtain

$$k_{1,0} = [\mathrm{Ar}]1.26\cdot10^{28}\ (T/300\mathrm{K})^{-8.7}\exp(-36660\ \mathrm{K}/T)\ \mathrm{cm^3\ mol^{-1}\ s^{-1}} \quad (17)$$

The fitted β_c corresponds to a temperature independent $-\langle\Delta E(E_0)\rangle \approx 250\ \mathrm{cm^{-1}}$. One would have expected a somewhat smaller value. However, because there are some uncertainties in the quantities entering $k_{1,0}$, the fitted β_c appears of acceptable magnitude. In any case, the fitted $k_{1,0}$ will serve well for data representation over the range 1100−1600 K studied here.

3.4. FALLOFF CURVES

We describe the transition of k_1 (analogous for k_2) from the low-pressure value $k_{1,0}$ to the high-pressure value $k_{1,\infty}$ by the falloff expression

$$k_1/k_{1,\infty} \approx [x/(1+x)]\ F(x) \quad (18)$$

where $x = k_{1,0}/k_{1,\infty}$. Broadening factors $F(x)$ are taken from the treatment of refs 45−47. The essential quantity entering $F(x)$ is the center broadening factor, F_{cent}, which in principle requires a treatment by full unimolecular rate theory; however, at this stage, the simplified method from ref 46 appears adequate enough. Combining strong collision and weak collision contributions leads to $F_{cent} \approx 0.10$ over the range 1000−2000 K. F_{cent} increases with decreasing temperatures below about 1400 K (see Table 3; an approximate representation of F_{cent} was derived to be $F_{cent} \approx 0.91\exp(-T/250\ \mathrm{K}) + 0.09\exp(-T/12500\ \mathrm{K}) + \exp(-7400\ \mathrm{K}/T)$.

dx.doi.org/10.1021/jp408363s | J. Phys. Chem. A 2013, 117, 11420−11429

Table 3. Modeled Low-Pressure Rate Constants for $C_2F_4 \rightarrow 2CF_2$ and Contributing Factors[a]

T/K	Z_{LJ}/cm^3 mol^{-1} s^{-1}	Q_{vib} (C_2F_4)	F_{rot}	F_E	β_c	$k_{1,0}$/[Ar] cm^3 mol^{-1} s^{-1}
1000	$2.45\cdot10^{14}$	$1.38\cdot10^{3}$	2.17	1.36	0.16	$1.3\cdot10^{7}$
1250	$2.63\cdot10^{14}$	$7.11\cdot10^{3}$	1.98	1.48	0.12	$2.2\cdot10^{9}$
1500	$2.77\cdot10^{14}$	$3.07\cdot10^{4}$	1.78	1.60	0.10	$5.1\cdot10^{10}$
1750	$2.91\cdot10^{14}$	$1.14\cdot10^{5}$	1.62	1.80	0.086	$3.7\cdot10^{11}$
2000	$3.04\cdot10^{14}$	$3.74\cdot10^{5}$	1.49	2.00	0.074	$1.4\cdot10^{12}$

[a]See text.

Table 4. Summary of Recommended Rate and Equilibrium Constants for $C_2F_4 \Rightarrow 2CF_2$[a]

$$K_c/\text{mol cm}^{-3} = 7.56\cdot10^{5}\,(T/300\text{ K})^{-2.4}\,\exp(-35050\text{ K}/T)$$

$$k_{1,\infty}/\text{s}^{-1} = 1.71\cdot10^{16}\,(T/300\text{ K})^{-0.87}\,\exp(-35050\text{ K}/T)$$

$$k_{1,0}/\text{s}^{-1} = [\text{Ar}]1.26\cdot10^{28}\,(T/300\text{ K})^{-9.70}\,\exp(-36660\text{ K}/T)$$

$$F_{cent} \approx 0.91\,\exp(-T/250\text{ K}) + 0.09\,\exp(-T/12500\text{ K}) + \exp(-7400\text{ K}/T)$$

$$k_{2,\infty}/\text{cm}^3\text{ mol}^{-1}\text{ s}^{-1} = 2.26\cdot10^{10}\,(T/300\text{ K})^{1.53}$$

$$k_{2,0}/\text{cm}^3\text{ mol}^{-1}\text{ s}^{-1} = [\text{Ar}]4.40\cdot10^{21}\,(T/300\text{ K})^{-6.7}$$

[a]See text.

For higher precision, one has to account for unsymmetries of the broadening factors, that is, $F(x) \neq F(-x)$, such as elaborated in refs 45−47. Here, one is in a certain dilemma. On one hand, one may fit the experimentally observed part of the falloff curve with the simple symmetric broadening factor from ref 42, given by

$$F(x) \approx F_{cent}^{1/[1+(\log x/N)^2]} \quad (19)$$

with $N \approx 0.75 - 1.27 \log F_{cent}$. Within experimental scatter, this equation provides satisfactory representations of the experimental falloff curves. These are included in Figures 6−8. On the other hand, one may use one of the relationships for unsymmetric broadening factors given in refs 42,45−47. For example, one may use

$$F(x) = 1 - (1 - F_{cent})\,\exp\{-[\log(1.5x)/N]^2/N^*\} \quad (20)$$

with N as in eq 19, $N^* = 2$ for $\log(1.5x) > 0$ and $N^* = 2[1 - 0.15\,\log(1.5x)]$ for $\log(1.5x) < 0$, given by eq 6.3 from ref 45. A representation with eq 20 is also included in Figures 6−8. The "wiggles" of the modeled falloff curves then are artifacts encountered when F_{cent} becomes very low, such as observed here. In addition, eqs 19 and 20 require a different fitted $k_{1,0}$, about 2−3 times larger for a fit with eq 19 than with eq 20. Nevertheless, in both cases, modeled and experimental falloff curves agree within experimental scatter. New unsymmetric expressions for $F(x)$, avoiding "wiggles" and leading to different extrapolated low-pressure rate constants, have been elaborated in ref 48.

Experimental high-pressure recombination rate constants from refs 4 and 10−12 agree well with our modeling results without any fitting being made (see Figure 13); however, our modeling of falloff curves for 873 K, using low-pressure dissociation rate constants, such as fitted in our experiments above 1100 K, does not reproduce the observed falloff of k_2 from ref 4. To meet the data from ref 4, one would have to increase $k_{2,0}$ at 873 K considerably, which can be ruled out for theoretical reasons. According to our modeling for the pressures of ref 4 and 873 K, there should have been a stronger falloff than observed. At this stage, we cannot explain this discrepancy.

Table 4 provides a summary of the modeled rate constants of the present work. Although modeled high-pressure rate constants without fitting are consistent with experimental dissociation and recombination results, rate constants in the falloff and low-pressure range require fitting of collision efficiencies. Although the experimental falloff curves for dissociation over the range 1100−1600 K are well reproduced, we note that the fitted average energy transferred per collision is higher than expected. Furthermore, there is the mentioned problem with low-temperature recombination falloff, such as measured in ref 4. Clarifications of these two aspects, therefore, appear desirable.

4. CONCLUSIONS

The present work on one hand provides a compact representation of rate constants for the reactions $C_2F_4 \Leftrightarrow 2CF_2$ over the full falloff curves and temperature range of experimental interest (see Table 4). With a value of the C_2F_4 dissociation energy of $E_0 = \Delta H^0_{R,0} = 67.5 \pm (0.5)$ kcal mol^{-1}, an intrinsically consistent analysis of experimental rate constants and equilibrium constants was achieved. The representation of the high-pressure rate constants was based on a complete, although only semiquantitative, theoretical modeling without using fit parameters. This analysis clearly reveals the reason for the unusually small recombination rate constants and their temperature dependence. This is the exceptionally strong anisotropy of the potential energy surface, which leads to a marked dynamical hindrance of the $CF_2 + CF_2$ association process. We characterized this by an unusually small ratio $\alpha/\beta \approx 0.23$ of the characteristic anisotropy (α) and Morse (β) parameters of the potential. The derived value for E_0 is in better accord with recent ab initio calculations, such as refs 23−27, than with the average of "experimental values" (see summary in ref 40).

APPENDIX: MOLECULAR PARAMETERS USED IN MODELING

Vibrational frequencies (in cm^{-1}). C_2F_4: 190, 218, 394, 406, 508, 551, 558, 778, 1186, 1337, 1340, 1872, from ref 18. CF_2: 666.3, from ref 31; 1114.4, 1225.1, from ref 32.

Rotational constants (in cm^{-1}). C_2F_4: 0.0687, 0.110, 0.183, $\sigma = 4$, from ref 18. CF_2: 0.368, 0.420, 2.951, $\sigma = 2$, from ref 33; g_{el} (CF_2) = 1.

Dissociation energy (in kcal mol^{-1}). 67.5 (±0.5) (see text).

dx.doi.org/10.1021/jp408363s | J. Phys. Chem. A 2013, 117, 11420−11429

Lennard-Jones parameters. σ_{LJ} (C_2F_4) = 0.468 nm, σ_{LJ} (Ar) = 0.347 nm, ϵ/k (C_2F_4) = 235.9 K, ϵ/k (Ar) = 114 K, from ref 49.

AUTHOR INFORMATION

Corresponding Author

*E-mail: shoff@gwdg.de.

Notes

The authors declare no competing financial interest.

ACKNOWLEDGMENTS

A. E. Croce gratefully acknowledges an extended Alexander-von-Humboldt fellowship.

REFERENCES

(1) Just, Th.; Roth, P.; Damm, R. Production of Hydrogen Atoms During the Thermal Dissociation of Ethylene Between 1700 and 2200 K. *Proc. Combust. Inst.* **1977**, *16*, 961−968.

(2) Cobos, C. J.; Croce, A. E.; Luther, K.; Troe, J. Temperature and Pressure Dependence of the Reaction $2CF_3$ (+ M) ⇔ C_2F_6 (+ M). *J. Phys. Chem. A* **2010**, *114*, 4748−4754.

(3) Hippler, H.; Luther, K.; Ravishankara, A. R.; Troe, J. High-Pressure Effects in the Recombination Reaction $CH_3 + CH_3 \rightarrow C_2H_6$. *Z. Phys. Chem. NF* **1984**, *142*, 1−13.

(4) Battin-Leclerc, F.; Smith, A. P.; Hayman, G. D.; Murrells, T. P. Kinetics of the Self-Reaction of CF_2 Radical and its Reaction with H_2, O_2, CH_4 and C_2H_4 over the Temperature Range 295−873 K. *J. Chem. Soc. Faraday Trans.* **1996**, *92*, 3305−3313.

(5) Schug, K. P.; Wagner, H. Gg. Der thermische Zerfall von C_2F_4 in der Gasphase. Zur Bildungsenthalpie von Difluorcarben. *Ber. Bunsenges. Phys. Chem.* **1978**, *82*, 719−725.

(6) Edwards, J. W.; Small, P. A. Kinetics of Pyrolysis of Chlorodifluoromethane. *Ind. Eng. Chem. Fundam.* **1965**, *4*, 396−400.

(7) Modica, A. P.; LaGraff, J. E. Decomposition and Oxidation of C_2F_4 Behind Shock Waves. *J. Chem. Phys.* **1965**, *43*, 3383−3392.

(8) Modica, A. P.; LaGraff, J. E. C_2F_4 Dissociation in Nitrogen Shocks. *J. Chem. Phys.* **1966**, *45*, 4729−4733.

(9) Carlson, G. A. Shock Tube Study of the Tetrafluoroethylene−Difluoromethylene Equilibrium. *J. Phys. Chem.* **1971**, *75*, 1625−1631.

(10) Dalby, F. W. Flash Photolysis Measurement of the Kinetics of CF_2 Reactions. *J. Chem. Phys.* **1964**, *41*, 2297−2303.

(11) Tyerman, W. J. R. Rate Parameters for Reactions of Ground-State Difluorocarbene and Determination of the Absolute Intensity of the $\tilde{A}^1B_1$−X^1A_1 Absorption Bands. *J. Chem. Soc. Faraday Trans.* **1969**, *65*, 1188−1198.

(12) Sharpe, S.; Hartnett, B.; Sethi, H. S.; Sethi, D. S. J. Absorption Cross Sections of CF_2 in the $A\,^1B_1$−$X\,^1A_1$ Transition at 0.5 nm Intervals and Absolute Rate Constant for $2CF_2 \rightarrow C_2F_4$ at 298 ± 3 K. *J. Photochem.* **1987**, *38*, 1−13.

(13) Martinez, R. I.; Huie, R. E.; Herron, J. T.; Braun, W. Infrared-Laser Photolysis/Mass Spectrometry. A Technique for the Real-Time Study of Free-Radical Kinetics, and its Application to the Reaction $2CF_2 \rightarrow C_2F_4$. *J. Phys. Chem.* **1980**, *84*, 2344−2347.

(14) Sarkar, S. K.; Palit, D. K.; Rao, K. V. S. R.; Mittal, J. P. Real-Time Observation of CF_2 Formation in the Infrared Multiple-Photon Dissociation of Fluoroform-d. *Chem. Phys. Lett.* **1986**, *131*, 303−309.

(15) Chowdhury, P. K.; Pola, J.; Rao, K. V. S. R.; Mittal, J. P. TEA CO_2 Laser Driven Oxidation of Tetrafluoroethene and Decafluorocyclopentane with Molecular Oxygen. Evidence for the Dioxetane Mechanism. *Chem. Phys. Lett.* **1987**, *142*, 252−254.

(16) Chowdhury, P. K.; Rao, K. V. S. R.; Mittal, J. P. Infrared Laser Induced Multiphoton Dissociation of Decafluorocyclopentane in a Concerted Pathway: Time-Resolved Evidence of Difluorocarbene Formation. *J. Phys. Chem.* **1988**, *92*, 102−106.

(17) Modica, A. P. Electronic Oscillator Strength of Difluoromethylene. *J. Phys. Chem.* **1968**, *72*, 4594−4598.

(18) NIST-JANAF Thermochemical Tables. *J. Phys. Chem. Ref. Data Monograph No. 9*; Chase, M. W., Ed.; American Institute of Physics: Woodbury, New York, 1998.

(19) *NASA-JPL Publication 10-6, Evaluation 17*; Jet Propulsion Labortatory, California Institute of Technology: Pasadena, CA, June 2011.

(20) Burcat, A.; Ruscic, B. *Third Millenium Ideal Gas and Condensed Phase Thermochemical Data Base for Combustion with Updates from Active Thermochemical Tables (ANL-05/20, TAE 960)*; Argonne National Laboratory: Lemont, IL, Sept. 2005)

(21) Goos, E.; Burcat, A.; Ruscic, B. *Extended Third Millenium Ideal Gas and Condensed Phase Thermochemical Data Base for Combustion with Updates from Active Thermochemical Tables*; ftp.technion.ac.il/pub/supported/aetdd/thermodynamics; July 2013.

(22) Klopper, W.; Ruscic, B.; Tew, D. P.; Bischoff, F. A.; Wolfsegger, S. Atomization Energies from Coupled-Cluster Calculations Augmented with Explicitly-Correlated Perturbation Theory. *Chem. Phys.* **2009**, *356*, 14−24.

(23) Feller, D.; Peterson, K. A.; Dixon, D. A. Ab Initio Coupled Cluster Determination of the Heats of Formation of $C_2H_2F_2$, C_2F_2, and C_2F_4. *J. Phys. Chem. A* **2011**, *115*, 1440−1451.

(24) Dixon, D. A.; Feller, D. Heats of Formation of CF_2, FCO, and CF_2O. *J. Phys. Chem. A* **1998**, *102*, 8209−8216.

(25) Demaison, J.; Margulès, L.; Martin, J. M. L.; Boggs, J. E. Anharmonic Force Field, Structure, and Thermochemistry of CF_2 and CCl_2. *Phys. Chem. Chem. Phys.* **2002**, *4*, 3282−3288.

(26) Schwartz, M.; Marshall, P. An Ab Initio Investigation of Halocarbenes. *J. Phys. Chem.. A* **1999**, *103*, 7900−7906.

(27) Sendt, K.; Bacskay, G. B. Spectroscopic Constants of the $\tilde{X}(^1A_1)$, $(^3B_1)$, and $(^1B_1)$ States of CF_2, CCl_2, and CBr_2 and Heats of Formation of Selected Halocarbenes: An Ab Initio Quantum Chemical Study. *J. Chem. Phys.* **2000**, *112*, 2227−2239.

(28) Kappel, Ch.; Luther, K.; Troe, J. Shock Wave Study of the Unimolecular Dissociation of H_2O_2 in Its Falloff Range and of Its Secondary Reactions. *J. Phys Chem. Chem. Phys.* **2002**, *4*, 4392−4398.

(29) Cobos, C. J.; Croce, A. E.; Luther, K.; Troe, J. Shock Wave Study of the Thermal Decomposition of CF_3 and CF_2 Radicals. *J. Phys. Chem. A* **2010**, *114*, 4755−4761.

(30) Astholz, D. C.; Brouwer, L.; Troe, J. High Temperature Ultraviolet Absorption Spectra of Polyatomic Molecules in Shock Waves. *J. Ber. Bunsenges. Phys. Chem.* **1981**, *85*, 559−564.

(31) Qian, H.-B.; Davies, P. B. Infrared Laser Spectroscopy of the ν_2 Band of Difluorocarbene (CF_2). *J. Mol. Spectrosc.* **1995**, *169*, 201−210.

(32) Burkholder, J. B.; Howard, C. J.; Hamilton, P. A. Fourier Transform Spectroscopy of the ν_1 and ν_3 Fundamental Bands of CF_2. *J. Mol. Spectrosc.* **1988**, *127*, 362−369.

(33) Marquez, L.; Demaison, J.; Boggs, J. E. Equilibrium C−F Bond Length and the Structure of Formyl Fluoride, Difluorocarbene, Monofluoromethylene, and Difluoromethane. *J. Phys. Chem. A* **1999**, *103*, 7632−7638.

(34) Skorobogatov, G. A.; Baranovskii, V. I. Ab Initio Calculation of Molecular, Thermodynamic, and Kinetic Parameters of CF, CF_2, CF_3, and C_2F_5 Radicals and CF_4, CF_3I, C_2F_4, and C_2F_6 Molecules in Gas. *Russ. J. Gen. Chem.* **2011**, *81*, 2262−2272.

(35) Maergoiz, A. I.; Nikitin, E. E.; Troe, J.; Ushakov, V. G. Classical Trajectory and Statistical Adiabatic Channel Study of the Dynamics of Capture and Unimolecular Bond Fission. V. Valence Interactions Between Two Linear Rotors. *J. Chem. Phys.* **1998**, *108*, 9987−9998.

(36) Frisch, M. J.; Trucks, G. W.; Schlegel, H. B.; Scuseria, G. E.; Robb, M. A.; Cheeseman, J. R.; Scalmani, G.; Barone, V.; Mennucci, B.; Petersson, G. A.; et al. *Gaussian 09, Revision A.02*; Gaussian, Inc.: Wallingford, CT, 2009.

(37) DeAlti, G.; Galasso, V.; Costa, G. Potential Energy Constants, Mean-Square Amplitudes of Vibration and Rotational Distortion Constants for C_2F_4, C_2Cl_4 and C_2Br_4. *Spectrochim. Acta* **1965**, *21*, 649−658.

(38) Quack, M.; Troe, J. Specific Rate Constants of Unimolecular Processes II. Adiabatic Channel Model. *Ber. Bunsenges. Phys. Chem.* **1974**, *78*, 240−252.

(39) Cobos, C. J.; Troe, J. Theory of Thermal Unimolecular Reactions at High Pressures. II. Analysis of Experimental Results. *J. Phys. Chem.* **1985**, *83*, 1010−1015.
(40) Poutsma, M. L. Chain Elongation During Thermolysis of Tetrafluoroethylene and Hexafluoropropylene: Modeling of Mechanistic Hypotheses and Elucidation of Data Needs. *J. Anal. Appl. Pyrolysis* **2011**, *92*, 25−42.
(41) Suzuki, C.; Sasaki, K.; Kadota, K. Rate Coefficient for Self-Association Reaction of CF_2 Radicals Determined in the Afterglow of Low-Pressure C_4F_8 Plasmas. *Plasma Chem. Plasma Process.* **2001**, *21*, 139−147.
(42) Troe, J. Predictive Possibilities of Unimolecular Rate Theory. *J. Phys. Chem.* **1979**, *83*, 114−126.
(43) Troe, J. Simplified Models for Anharmonic Numbers and Densities of Vibrational States. I. Application to NO_2 and H_3^+. *Chem. Phys.* **1995**, *190*, 381−391.
(44) Troe, J.; Ushakov, V. G. Anharmonic Rovibrational Numbers and Densities of States for HO_2, H_2CO, and H_2O_2. *J. Phys. Chem. A* **2009**, *113*, 3940−3945.
(45) Troe, J.; Ushakov, V. G. Revisiting Falloff Curves of Thermal Unimolecular Reactions. *J. Chem. Phys.* **2011**, *135*, 054304-1−054304-10.
(46) Troe, J. Theory of Thermal Unimolecular Reactions in the Fall-Off Range. I. Strong Collision Rate Constants. *Ber. Bunsenges. Phys. Chem.* **1983**, *87*, 161−169.
(47) Gilbert, R. G.; Luther, K.; Troe, J. Theory of Thermal Unimolecular Reactions in the Fall-Off Range. II. Weak Collision Rate Constants. *Ber. Bunsenges. Phys. Chem.* **1983**, *87*, 169−177.
(48) Troe, J.; Ushakov, V. G., Representation of "Broad" Falloff Curves for Dissociation and Recombination Reactions. *Z. Phys. Chem.* submitted Oct 2013.
(49) Hippler, H.; Wendelken, H. J.; Troe, J. Collisional Deactivation of Vibrationally Highly Excited Polyatomic Molecules. II. Direct Observations for Excited Toluene. *J. Chem. Phys.* **1983**, *78*, 6709−6718.